HORIZON 2020

The EU Framework Programme for Research and Innovation

H2020-EO-1-2014

Pixel based sensible (QH) and latent (QE) heat fluxes

Deliverable D6.1

URBANFLUXES

URBAN ANTHROPOGENIC HEAT FLUX FROM EARTH OBSERVATION SATELLITES

LEAD AUTHOR

Christian Feigenwinter (UNIBAS)

AUTHORS

Andreas Wicki (UNIBAS)

CONTRIBUTORS

Eberhard Parlow (UNIBAS), Roland Vogt (UNIBAS), Wieke Heldens (DLR), Fabio del Frate (GEO-K), Fredrik Lindberg (UoG), Frans Olofson (UoG), Zina Mitraka (FORTH), Nektarios Chrysoulakis (FORTH), Sue Grimmond (UoR), Judith Klostermann (ALTERRA)

DATE

3 February 2016

ISSUE

1.0

GRANT AGREEMENT

no 637519

DISSEMINATION LEVEL

PU

CONTENTS

LIST OF FIGURES

LIST OF TABLES

1 INTRODUCTION

1.1 Purpose of the document

This document is the Deliverable 6.1 of the URBANFLUXES (URBan ANthropogenic heat FLUX from Earth observation Satellites) Project. It contains the progress on the estimation of sensible and latent heat flux Q_E and Q_H on a pixel base within WP6. Methods are explained and then applied to the case study of Basel. The application to London and Heraklion will be included in deliverable D6.2 by M18 when the required data are available. It also includes an overview of the URBANFLUXES project as a whole.

1.2 Definitions and acronyms

Acronyms

ARM	Aerodynamic Resistance Method
CoP	Community of Practice
DEM	Digital Elevation Model
DSM	Digital Surface Model
DSS	Decision Support System
EO	Earth Observation
EC	Eddy Covariance
FAI	Frontal Area Index
LCZ	Local Climate Zones
LHA	Lufthygiene Amt (Service for air pollution)
LST	Land Surface Temperature
LULC	Land Use / Land Cover
MB	Management Board
MOST	Monin-Obukhov Similarity Theory
PAR	Photosynthetic Active Radiation
PAI	Plan Area Index
UEB	Urban Energy Budget
UMEP	Urban Multi-scale Environmental Predictor
URBANFLUXES	URBan ANthropogenic heat FLUX from Earth observation Satellites
WP	Work Package

1.3 Document references

[R1] URBANFLUXES Grant Agreement, n. 637519, 2/11/2014

[R2] URBANFLUXES Deliverable D.3.1 Urban Surface morphology land cover/use and characteristics, DEC 2015

[R3] URBANFLUXES Deliverable D.3.2.1 Preliminary LCZ classification, DEC 2015

[R4] URBANFLUXES Deliverable D.5.1 Spatial assessment of heat storage flux, DEC 2015

2 Project Overview

The anthropogenic heat flux (Q_F) is the heat flux resulting from vehicular emissions, space heating and cooling of buildings, industrial processing and the metabolic heat release by people. Both urban planning and Earth system science communities need spatially disaggregated Q_F data, at local (neighbourhood, or areas larger than the order of 100 m x 100 m) and city scales. Such information is practically impossible to derive by point *in-situ* fluxes measurements, while satellite remote sensing is a valuable tool for estimating Urban Energy Budget (UEB) parameters exploiting Earth Observation (EO) data. While the estimation of Q_F spatial patterns by current EO systems is a scientific challenge, the major challenge lies on the innovative exploitation of the Copernicus Sentinels synergistic observations to estimate the spatiotemporal patterns of Q_F and all other UEB fluxes.

The main goal of URBANFLUXES is to investigate the potential of EO to retrieve Q_F, supported by simple meteorological measurements. The main research question addresses whether EO is able to provide reliable estimates of Q_F for the time of the satellite acquisition. URBANFLUXES answers this question by investigating the potential of EO to retrieve Q_F spatial patterns, by developing a method capable of deriving Q_F from current and future EO systems. URBANFLUXES aims to develop an EO-based methodology easily transferable to any urban area and capable of providing Q_F benchmark data for different applications. URBANFLUXES is expected to increase the value of EO data for scientific analyses and future emerging applications (such as urban planning and local/regional level climate change mitigation/adaptation), by exploiting the improved data quality, coverage and revisit times of the Copernicus Sentinels data. To this end, the specific objectives of the project are:

- to improve the accuracy of the radiation balance spatial distribution calculation;
- to develop EO-based methods to estimate the flux of heat storage in the urban fabric, as well as the turbulent sensible and latent heat fluxes at local scale;
- to employ energy budget closure to estimate the anthropogenic heat flux patterns;
- to specify and analyse the uncertainties associated with the derived products;
- to evaluate the products by comparisons with Q_F estimations by independent methods;
- to improve the understanding of the impact of Q_F on urban climate; and to communicate this understanding to the urban planning community, which will in turn lead to a better understanding of what new knowledge is needed on the ground;
- to exploit Sentinels 2 and 3 synergistic observations to retrieve UEB fluxes at the local scale, with the frequency of the Sentinel 3 series acquisitions.
- to standardise the resulting products, and by organizing an effective dissemination mechanism, to enhance their use by urban planners and decision makers in cities, as well as by EO scientists, Earth system modellers and urban climatologists.

The duration of URBANFLUXES is three years and it is divided into two main phases: during the 1st Phase an analysis method is being developed to estimate Q_F spatial patterns using currently available satellite data; during the 2nd Phase the developed method will be adapted to Sentinels synergy to derive Q_F spatiotemporal patterns. Three different urban areas are selected in URBANFLUXES as case studies: a highly urbanized mega city (London); a typical central European medium size city, that requires a substantial amount of energy for heating (Basel); and a smaller, low latitude Mediterranean city that requires a substantial amount of energy for cooling (Heraklion). The project uses a Community of Practice (CoP) approach, which means that in the case studies, local stakeholders and scientists meet on a regular basis to learn from each other and to make clear what aspects are important for the future users of the URBANFLUXES products.

URBANFLUXES is expected to generate a novel analysis method for estimation of UEB components from Copernicus data, enabling its integration into applications and operational services; for example to: develop rules of thumb for density and green space ratio, distinguish between insulated and non-insulated buildings and evaluate the implementation of climate change mitigation technologies, such as solar-screening and green-belting.

Despite its local importance, Q_F is omitted from climate models simulations. Observations of global temperature evolution indicate a pronounced warming over the last 150 years, with an increase in the occurrence of heat waves. The added value and benefit expected to emerge from URBANFLUXES is therefore related to quality of life, because it is expected to improve our understanding of the contribution of Q_F to heat wave intensity and thus to allow insight into strategies for mitigation. Q_F estimates are needed for all cities to be able to document the magnitude of the fluxes effects on urban climate so that the impact of Q_F can be included in climate modelling. URBANFLUXES is therefore expected to advance the current knowledge of the impacts of Q_F on urban heat island and hence on urban climate, and consequently on energy consumption in cities. This will lead to the development of tools and strategies to mitigate these effects, improving thermal comfort (social benefit) and energy efficiency (economic benefit). The long term operation of the Sentinels series guarantees the future supply of satellite observations, providing the means for the development and realization of the URBANFLUXES methodology.

URBANFLUXES is expected to support sustainable planning strategies relevant to climate change mitigation and adaptation in cities, because knowledge of Q_F spatio-temporal patterns is important for urban planning (e.g. to reduce or prevent Q_F hot spots), health (e.g. to estimate the impact on thermal comfort) and future proofing (e.g. to plan and implement interventions towards Q_F reduction in these areas). Planning tools, such as Urban Climatic Maps and Climatope Maps, should be enriched with information on Q_F patterns. Mapping provides visualization of assessments of these phenomena to help planners, developers and policy makers make better decisions on mitigation and adaptation.

3 ESTIMATION OF SENSIBLE AND LATENT HEAT FLUX ON A PIXEL BASIS

3.1 Concept and approach

The turbulent heat fluxes of sensible Q_H and latent Q_E heat are strongly modified by the properties of the urban surface, i.e. 3D geometry, high roughness, impervious surfaces, complex source/sink distribution and injections of heat and water into the urban atmosphere by human activities (traffic, heating, waste management, etc.). The spatial variability of urban terrain complicates their estimation. The existence of various surface types and different exposures to solar radiation in a complex surface geometry can lead to significant variations in heat fluxes over short distances. This problem is well-known, but for practical purposes various simplifications that assume homogeneous properties at the surface like Monin–Obukhov Similarity Theory (MOST) are still widely used to estimate the sensible heat flux in meso-scale models, typically with the scalar roughness approach. Although MOST was originally derived for flat and homogeneous terrain, several studies have used it over heterogeneous terrain, including cities (Nadeau et al. 2009). In URBANFLUXES, the Aerodynamic Resistance Method (ARM) to estimate Q_H uses the simple relation (e.g. Brutsaert, 1982):

$$Q_H = \rho c_p \frac{T_s - T_a}{r_a} \quad , \tag{2}$$

where ρ is the density of air, c_p the specific heat of air at constant pressure, T_s is surface temperature that can be calculated from the satellite thermal infrared observations, T_a is the air temperature recorded by the meteorological stations, and r_a is the aerodynamic resistance. Analogously to Q_H, Q_E is expressed as:

$$Q_E = \frac{\rho c_p}{\gamma} \frac{e_s^* - e_a}{r_a + r_s} \quad , \tag{3}$$

where e_s^* is the saturation water vapour pressure at the surface temperature, e_a is the atmospheric water vapour pressure, γ is the psychrometric constant and r_s is the stomatal resistance. Stomatal resistance is calculated after Kato et al. (2008) using the simplified equation from Nishida et al. (2003):

$$\frac{1}{r_s} = \frac{f_1(T_a) f_2(PAR)}{r_{sMIN}} + \frac{1}{r_{cuticle}} \quad , \tag{4}$$

where PAR is the photosynthetic active radiation, r_{sMIN} is the minimum stomatal resistance and $r_{cuticle}$ is the canopy resistance related to the diffusion through the cuticle layer of leaves. Functions f_1 and f_2 are calculated as per Nishida et al. (2003) and r_{sMIN} can be determined for each vegetation type (Kato et al. 2008). Q_E is calculated by land cover type and weighted by fraction of water, vegetation and pervious surfaces with the respective r_{sMIN} in every pixel. The calculation of r_s by eq. (4) is documented in detail in section 4.3.5.

The aerodynamic resistance r_a for sensible heat in eq. (2) can then be written as (e.g. Voogt and Grimmond, 2000):

$$r_a = \frac{1}{u_* k}\left[ln\left(\frac{z_{ref}-z_d}{z_{0m}}\right) - \psi_h\left(\frac{z_{ref}-z_d}{L}\right) + \ln\left(\frac{z_{0m}}{z_{0h}}\right)\right] \quad (5)$$

and $$u_* = Uk\left[ln\left(\frac{z_{ref}-z_d}{z_{0m}}\right) - \psi_m\left(\frac{z_{ref}-z_d}{L}\right) - \psi_m\left(\frac{z_{0m}}{L}\right)\right]^{-1} \quad (6)$$

where u_* is the friction velocity, k is the von Karman constant (0.4), z_{ref} refers to a reference height (usually the height of wind measurements), z_d is the zero-plane displacement height, L is the Monin-Obukhov length, z_{0m} and z_{0h} are the roughness lengths and $\psi_{m,h}$ are the stability functions for momentum and heat, respectively. Equation (6) can be used to estimate u_* from wind velocity U, if no direct measurements of the friction velocity are available. z_{0h} values are usually reported as the dimensionless number $k\beta^{-1}$, defined as

$$k\beta^{-1} = ln\left(\frac{z_{0m}}{z_{0h}}\right) \quad (7)$$

In literature, reported values for $k\beta^{-1}$ show a large variability, even for similar types of surfaces. Lowest values of around 2 correspond to homogeneous vegetative surfaces (Brutsaert 1982), but also to flat semi-arid areas (Koshiek et al. 1993). Higher values are reported for heterogeneous surfaces and urban land use classes, e.g. with values around 20-27 for a light industrial site as reported by Voogt and Grimmond (2000). Kato and Yamaguchi (2007) list values for $k\beta^{-1}$ of 7 (industrial, urban, forest), 4.6 (grassland) and 3.9 (lawn, bare soil). Several studies used Eddy Covariance (EC) and/or scintillometry measurements to determine $k\beta^{-1}$ in the footprint of their measured fluxes. In URBANFLUXES this approach will be used later to evaluate results (D6.2). Here, we will use flux tower measurements as reference values for the magnitude of the fluxes of momentum and sensible and latent heat during the satellite overpass. z_{0h} was calculated from the roughness Reynold's number (see section 4.3.5 and Equation (14)).

To determine the input parameters for r_a, the approach of Xu et al. (2008) is modified to the satellite data. Both, roughness length (for heat and momentum) and displacement height are needed in r_a calculation. Input for the calculation of roughness parameters, i.e. the morphometry, is provided by [R2]. Roughness parameters are calculated using the real urban surfaces parameterization of Kanda et al. (2013) in section 4.3.4.

Consequently, the roughness length for Q_H and Q_E, as well as the minimum stomatal resistance for latent heat flux need to be interpolated based on the urban morphology and the urban surface characteristics as they will be derived from EO. Standard meteorological observations and direct measurements from EC flux towers will be used to support the turbulent fluxes estimation from EO data. These observations are necessary to calibrate and verify the satellite observations and include solar radiation, relative humidity, air pressure, air temperature and wind speed measured at representative locations in case study areas.

3.2 Input data

Surface characteristics in the form of morphology and atmospheric conditions are essential in the ARM-scheme. The following describes how to derive these parameters and the sources which are used (Table 2). The goal of URBANFLUXES is to resolve the UEB components at a resolution of 100 metre pixels (1 ha) across any urban area where the appropriate data are available [R1].

Upscaling of the fluxes to the total area will be accomplished through the classification of Local Climate Zones (LCZ) and/or other zoning techniques. See [R3] for further details.

Table 1. Data required for the estimation of sensible and latent heat flux by the ARM

Needed for WP6 D6.1	Source
Surface temperature (T_s)	EO
Atmospheric vapour pressure (e_a)	Sensor network
Air temperature (T_a)	Sensor network
- Saturation vapour pressure (e_s^*)	from T_a
Wind velocity, wind direction, friction velocity	Flux tower measurements
In-situ Q_H and Q_E for validation	Flux tower measurements
Roughness (z_{0m}, z_{0h}, z_d)	Morphometry, DSM & DEM
Plan area index (λ_p)	Morphometry, DSM & DEM
Frontal area index (λ_f)	Morphometry, DSM & DEM
Mean, max and stdev of building height (z_H, z_{Hmax}, z_{Hstd})	Morphometry, DSM & DEM
Aerodynamic resistances (r_a, r_s)	from morphometry, DSM & DEM, flux towers, EO, LULC, literature values for comparison

4 City scale sensible and latent heat flux: The Basel case study

4.1 Datasets

The estimation of sensible and latent heat flux is tested for the Basel case study on 30 AUG 2015 1116 CET from a Landsat 8 scene. The scene was chosen because high heat fluxes are expected. Results are presented for Basel test area with a 100 m grid to be compatible with [R4]. Note that some input parameters are derived from higher resolution datasets in order to profit from the higher accuracy.

4.2 Meteorological conditions, air temperature and humidity

The sensor network in Basel at the end of AUG 2015 (Table 3, Figure 2) was incomplete due to delivery problems and delays with permissions for the installation of stations. However, together with the permanent stations operated by UNIBAS and the service for air pollution (LHA), we have 13 locations with measurements of air temperature and humidity, including the two flux towers BKLI and BAES with other relevant variables (radiation, turbulent fluxes, friction velocity, etc.).

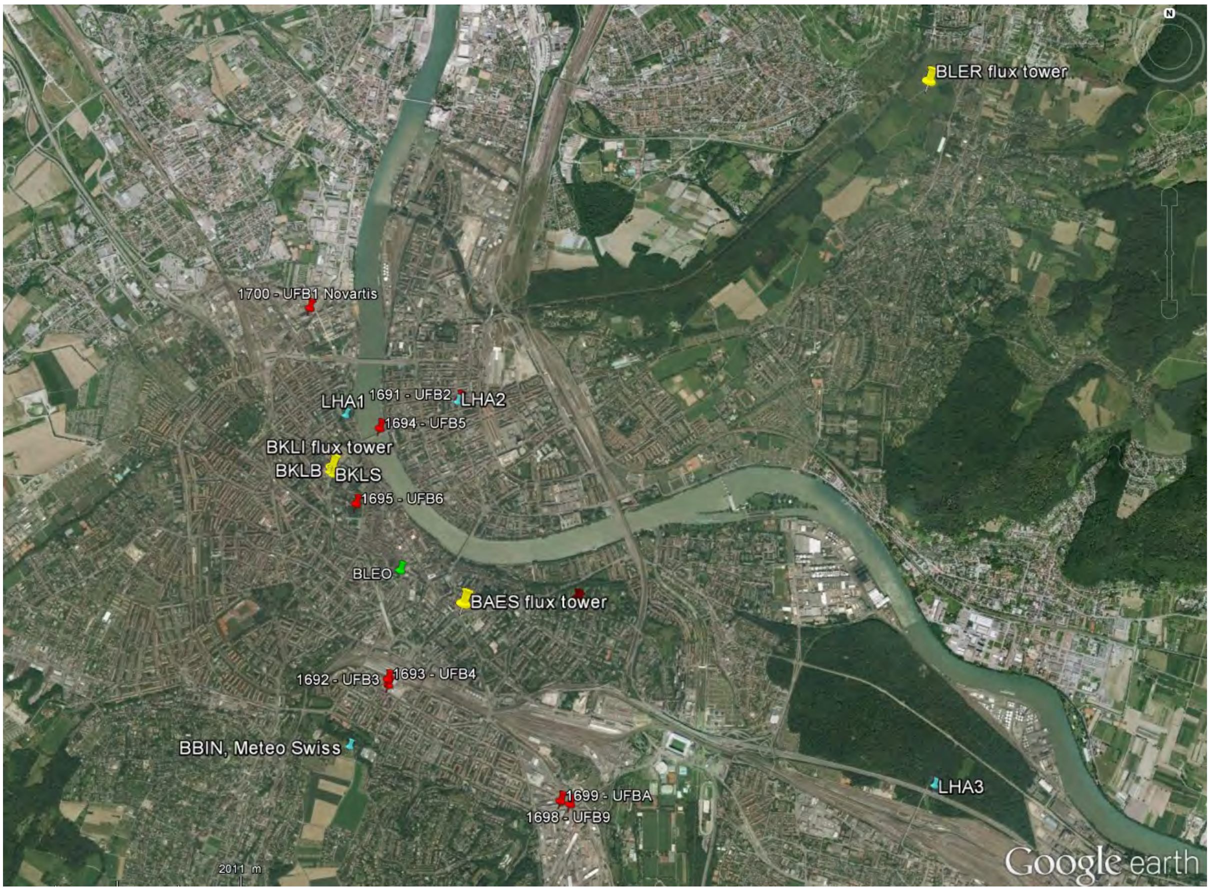

Figure 1: Locations of Basel sensor network stations. Refer to Tables 3 and 4 for more details and measurement values.

Meteorological conditions on 30 AUG 2015 1116 CET (Tables 3 and 4, Appendix) were very similar at the two flux towers (Table 4), except for latent heat flux, which is higher at BKLI due to larger vegetation fraction in the tower footprint. Flux footprints and source areas are subject to detailed investigation in D6.2 (*Verification, uncertainty analysis and documentation of EO derived Q_H and Q_E fluxes*). Measured air temperatures range from 29 to 32 °C, if the extreme value of 34 °C at LHA2 is not considered (Table 3). This station, operated by the air pollution service, is located in a sheltered, poorly ventilated location at street level and thus not representative of a larger area. Therefore an air temperature of 29.5 °C at the reference height for the whole Basel test area is used initially in Equation (2) and to calculate e_s for Equation (3). Relative humidity ranges from 30 to 38 % at city stations, at the rural reference site BLER (grassland) a value of 56% is measured. Therefore values of 41 hPa for e_s and 14 hPa for e_a, resulting in a vapour saturation deficit of 27 hPa, are used in Equation (3).

Table 2. Basel sensor network, data from stations shaded in grey were available on 30 AUG 2015. Grid coordinates are for UTM zone 31 N. Heights in metres are given both for above sea level (asl) and above ground level (agl), air temperature (*T*) and relative humidity (*RH*), where available.

Station	Code	east	north	Height asl (m)	Building height (m)	Height agl (m)	*T* (°C)	*RH* (%)
Basel-Binningen	BBIN	393386	5266268	316		2	29.7	38.0
Basel St. Johann	LHA1	393342	5269033	260		3	32.0	32.0
Feldberg street	LHA2	394303	5269133	256		3	34.0	29.0
Feldberg roof	UFB2	394322	5269151	256	15	2	31.5	35.0
A2 Hard	LHA3	398267	5265860	275		4, 15		
Chrischona	CRI	401255	5269534	636		100		
BKLI	BKLI	393221	5268560	286	21	18	29.5	37.5
BKLB	BKLB	393199	5268559	265		2	29.5	36.0
BKLS	BKLS	393235	5268536	264		2	30.0	35.7
BLER	BLER	398455	5271865	273		2	30.1	56.0
Bridge St.-Johann	UFB5	393614	5268899	256		4	29.2	37.0
SBB street	UFB4	393716	5266763	280		4	31.0	35.0
SBB roof	UFB3	393707	5266740	280	20	2	30.0	35.0
Gellert street	UFB8	395298	5267440	270				
Gellert roof	UFB7	395298	5267357	270	20	2		
Novartis roof	UFB1	393037	5269940	256	75	2		
Dreispitz roof	UFB9	395230	5265743	284	18	2		
Dreispitz street	UFBA	395148	5265773	284		3		
Petersplatz	UFB6	393421	5268262	268	25	5,15,24		
BAES	BAES	394330	5267379	270	36	6	29.5	37.5
BLEO	BLEO	393731	5267715	273	20	2	30.8	33.0

Table 3. Meteorological conditions at flux towers on 30 AUG 2015 1116 CET.
SW Short wave, LW Longwave ↓↑ incoming/outgoing

Variable (units)	BKLI	BAES	Range (all stations)	remarks
Radiation SW ↓↑ (W m^{-2})	761/ 87	770/ 83		
Radiation LW↓↑ (W m^{-2})	393/517	383/519		
Net radiation (W m^{-2})	550	554		
Sensible heat flux (W m^{-2})	177	190		
Latent heat flux (W m^{-2})	91	50		
Station pressure (hPa)	986	982		
Friction velocity (m s^{-1})	0.25	0.37		
Stability index $(z_{ref}-z_d)/L$	-2.2	-1.25		
Wind speed (m s^{-1})	1.8	1.6	0.5…1.7	
Wind direction	NW	NNE	S,W,NW	
Air temperature (°C)	29.5	29.5	29…34	34 at LHA2
Relative humidity (%)	37	37	30…56	56 at BLER

4.3 Land Surface Temperature LST

Surface temperatures (Figure 3), derived from the Landsat 8 Thermal Infrared Sensor (TIRS) for 30th of August 2015 at 1116 CET, were resampled to the test area grid. This data is provided by deliverable D3.1 using the methods outlined therein [R2]. The highest LSTs (up to 43 °C) were observed in the most densely built-up areas, the industrial regions and at railway stations. Water bodies, i.e. the river Rhine, and forests show the lowest LSTs.

4.4 Morphometry and roughness parameters z_d and z_{0m}

Morphometric parameters z_H, z_{Hmax}, z_{Hstd}, λ_p and λ_f were derived from 1 m x 1 m digital surface model (DSM) for the Basel test area using UMEP (Urban Multi-scale Environmental Predictor, Lindberg et al. 2015). See [R2] and [R4] for further detailed information about derivation of morphometric parameters and UMEP. Roughness parameters z_d and z_{0m} were then calculated according to Kanda et al. (2013), using the above morphometric values, a reference height of 4 m above the mean building height z_H and the modified Dyer (1974) stability functions from Högström (1988). The reference height of z_H + 4 m was chosen with the underlying assumption that this height must be somewhere close above mean roof level. Note that the following calculations are not very sensitive to this height within a range of a few meters.

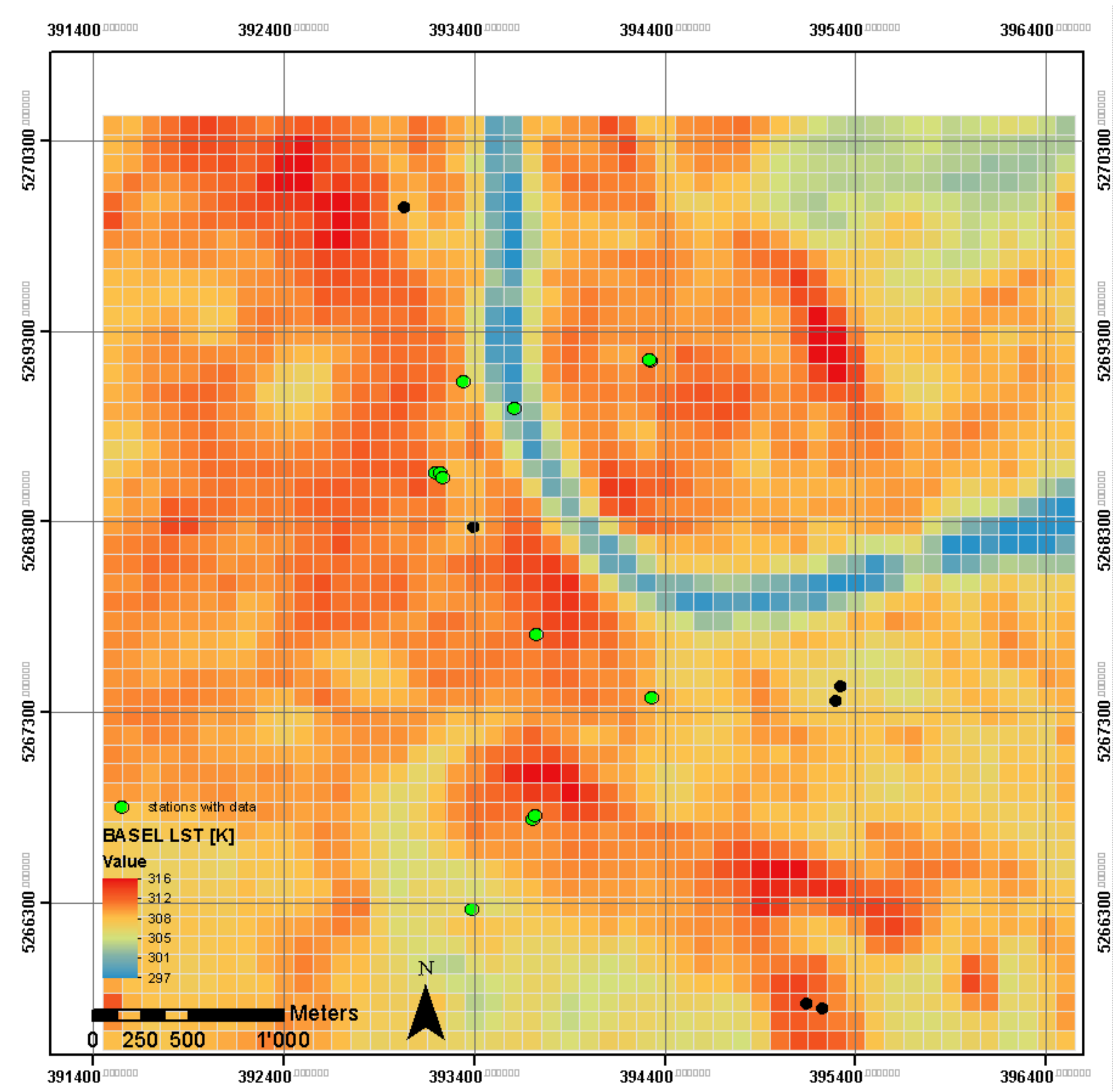

Figure 2. Surface temperatures derived from Landsat 8 scene 30 AUG 2015 1116 CET, resolution 100 m x 100 m (resampled from original 90 m resolution), stations with meteorological measurements (green dots), and inactive stations (black) at time of satellite overpass. Grids coordinates are for UTM zone 31 N.

The Kanda et al. (2013) modification to Macdonald (1998) is used with the real urban surfaces parameters. This uses mean building height z_H, its maximum z_{Hmax}, its standard deviation z_{Hstd}, plan area index λ_F and frontal area index λ_F. For the zero-plane displacement height z_d (Kanda et al. 2013):

$$\frac{z_d}{z_{Hmax}} = c_0 \mathrm{X}^2 + \left(a_0 \lambda_p^{b0} - c_0\right)\mathrm{X} \tag{8}$$

with $$X = \frac{z_{Hstd} + z_H}{z_{Hmax}}, \quad 0 \leq X \leq 1.0 \tag{9}$$

where a_0, b_0, and c_0 are the regressed constant parameters, i.e., 1.29, 0.36, and −0.17, respectively; and for the roughness length for momentum z_{0m} :

$$\frac{z_{0m}}{z_0(mac)} = b_1 Y^2 + c_1 Y + a_1 \tag{10}$$

where $$Y = \frac{\lambda_p z_{Hstd}}{z_H}, \quad Y \leq 0 \tag{11}$$

with the regression constants a_1 = 0.71, b_1 = 20.21 and c_1 = -0.77, and $z_0(mac)$ from the Macdonald (1998) equations:

$$\frac{d}{z_H} = 1 + A^{-\lambda_p}(\lambda_p - 1) \tag{12}$$

$$\frac{z_0(mac)}{z_H} = \left(1 - \frac{d}{z_H}\right) \exp\left[-\left\{0.5\beta \frac{c_{lb}}{k^2}\left(1 - \frac{d}{z_H}\right)\lambda_f\right\}^{-0.5}\right] \tag{13}$$

where A and β are parameters with values of 4.43 and 1.0, respectively, c_{lb} = 1.2 is the drag coefficient of an obstacle and k the von Karman constant (0.4).

The calculated z_d and z_{0m} (Equation 8 and 13) are shown in Figures 4 and 5.

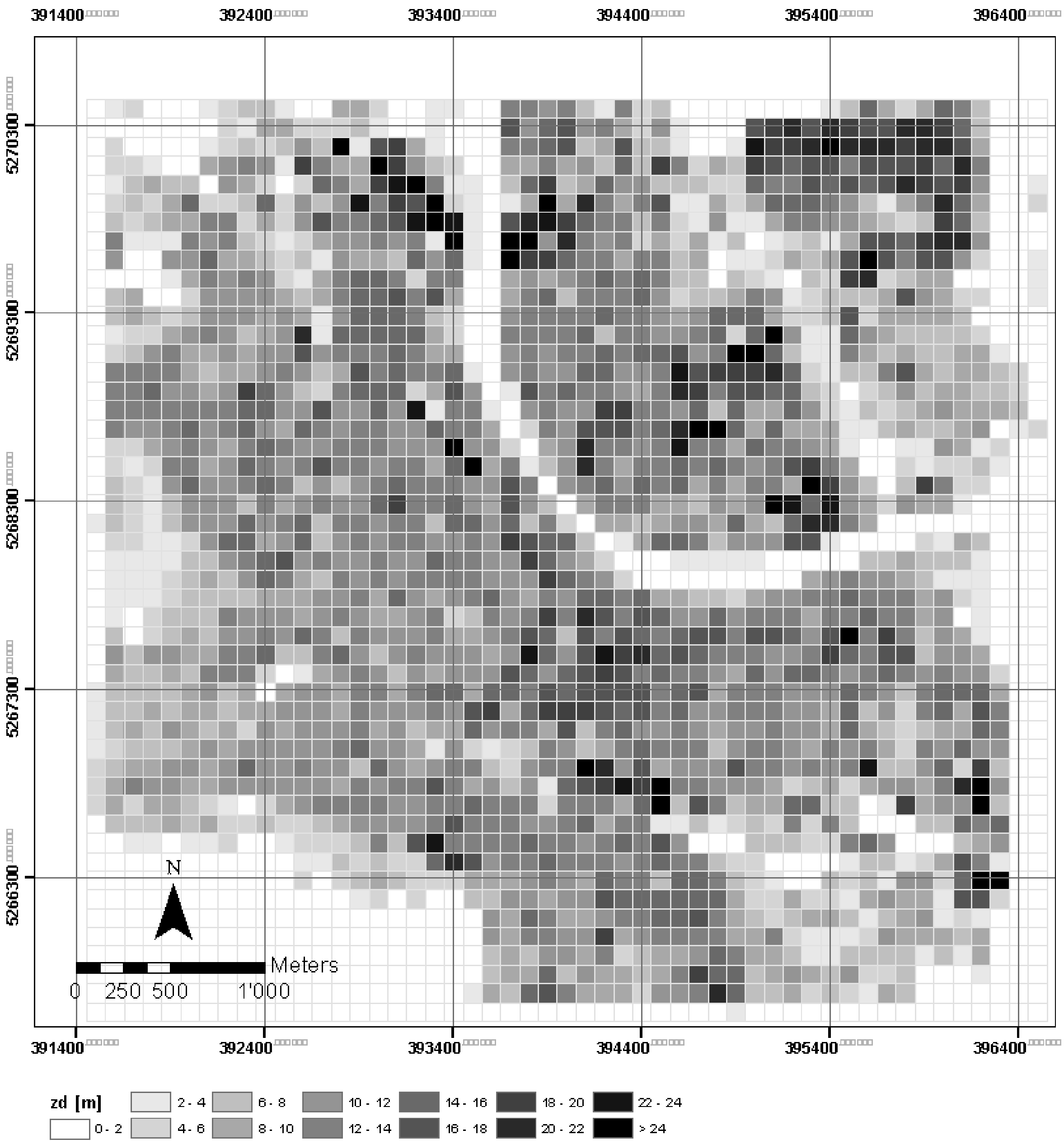

Figure 3. Zero-plane displacement height z_d as calculated by Equation (8).

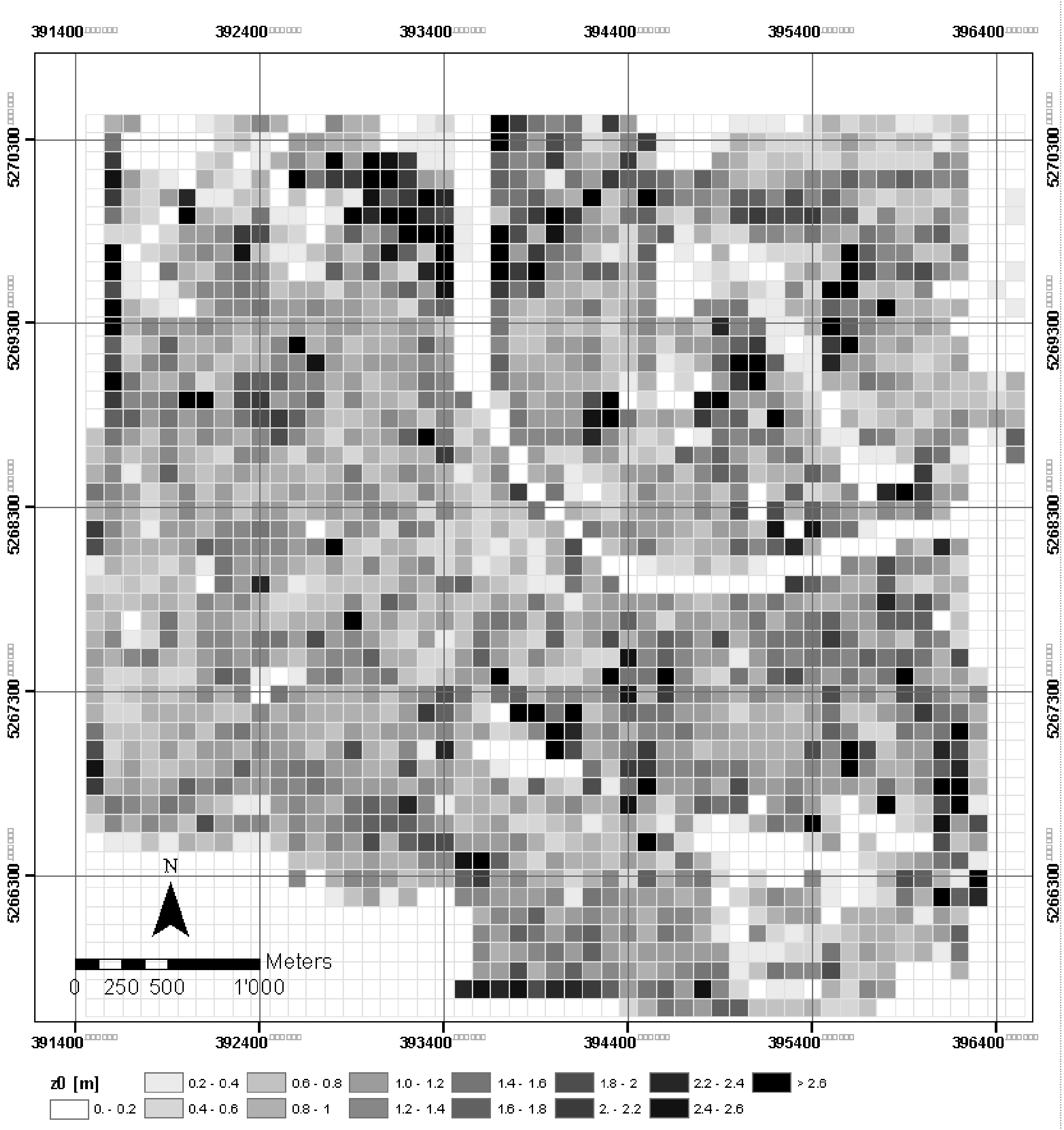

Figure 4. Roughness length for momentum z_{0m}

4.5 Aerodynamic resistances

Aerodynamic resistance for heat r_{ah} was calculated according to Equation (5) using the Brutsaert (1982) equation for the excess resistance z_{0h} when using radiometric temperatures. Here we apply the value of the coefficient α adapted to urban surfaces by Kanda et al. (2007) and Kanda and Moriizumi (2009):

$$z_{0h} = z_{0m}[7.4\, exp(-\alpha Re_*^{0.25})] \qquad (14)$$

where α = 1.29 and $Re_{*}=z_{0m}u_{*}/\nu$ is the roughness Reynolds number with a kinematic molecular viscosity ν of 1.461 × 10^{-5} ms^{-1}. This z_{0h} value is used in Equation (7) for the calculation of aerodynamic resistance r_{ah}. Values for r_{ah} are shown in Figure 6.

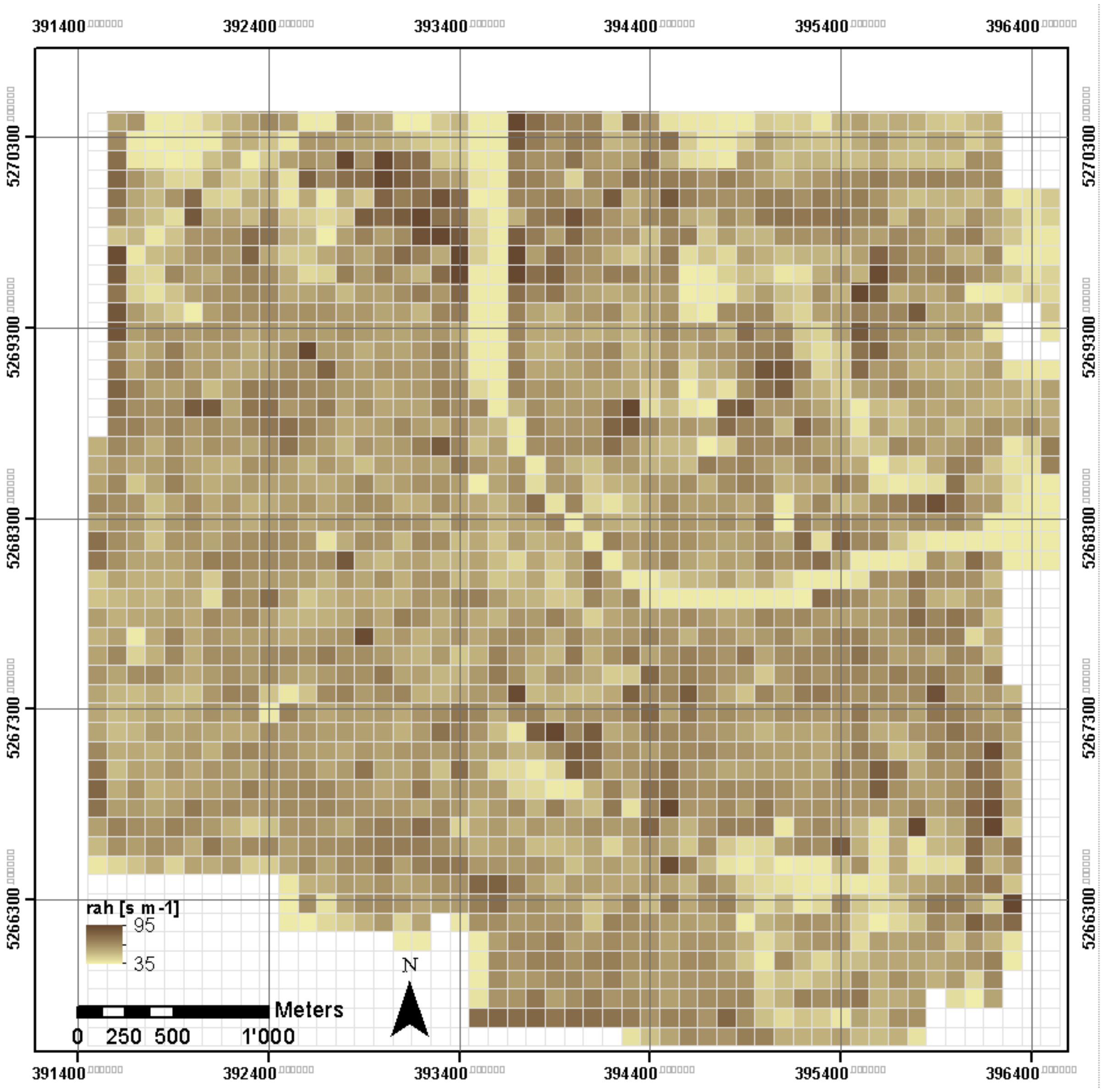

Figure 5. Aerodynamic resistance r_{ah} at the time of the overflight at reference height z_H + 4 m

Stomatal resistance r_s for vegetated surfaces is calculated by Equation (4) using the values for r_{sMIN} in Table 5. *PAR* was taken as $f * SW\downarrow$, the incoming shortwave radiation. For f we used 2.05 μmol m^{-2} s^{-1} as proposed by Nishida et al. (2007). The following relations apply for f_1 (T_a) and f_2 (*PAR*) in Equation (4):

$$f_1(T_a) = \left(\frac{T_a - T_n}{T_o - T_n}\right)\left(\frac{T_x - T_a}{T_x - T_o}\right)^{[(T_x - T_o)/(T_o - T_n)]} \quad (15)$$

where T_a is air temperature, T_n is the minimum (2.7 °C), T_O the optimal (31.1 °C) and T_x (45.3 °C) the maximum temperature for stomatal activity, respectively. $f_2(PAR)$ is calculated as $f_2(PAR) = (PAR)/(PAR+A)$, with A = 152 µmol m^{-2} s^{-1} as the parameter for photon absorption efficiency at low light intensity. This set of parameters is considered as representative for all biomes (Nishida et al. 2003) for the time being, but may be adapted to city specific conditions in further calculations of r_s.

4.6 Land cover fractions

To estimate Q_E fractions of transpiring surfaces are needed. In order to have the most precise information, multi-temporal pan-sharpened (Gram-Schmidt, 15 m pixels size) Landsat 8 scenes (YYYY-DOY: 2013-156, 2014-159, 2014-198, 2015-162, 2015-185, 2015-217, 2015-242) were used with the Maximum Likelihood Classifier. The modal value of the seven scenes was computed for every pixel containing a non-vegetation class. Thereafter, the "true" value of one pixel is taken to be with the highest mode class in this pixel. Vegetation classes are date specific. See Laben and Brower (2000) for a complete overview of the pan-sharpening method.

Land use classes were assigned based on *a priori* understanding of the city structure. "Dense Urban" covers the Basel old town with midrise buildings with low sky view factors and vegetation fractions. "Urban" areas have typical housing (3-6 stories) of the city with midrise buildings, medium size streets (15-25 m width) with larger sky view factors and with vegetation in the backyard of the buildings. The "Suburban" class includes individual low-rise buildings surrounded by small private gardens with smaller building fractions compared to "Urban". "Urban Rural" contains all types of urban gardening or graveyards. The two industrial classes are "Industrial 1" with large roads, rails and concrete squares (Roads/Rails/Concrete) and "Industrial 2" with large midrise to high-rise buildings, bright roofs and high imperviousness. The agricultural classes differ in the kind of cultivation. Wheat and other cereals that appear bright in an RGB image (Agriculture Yellow) were distinguished from corn, grass or other rather greenish plants (Agriculture Green). Vineyard/Shrub is concentrated on some hillside parts with large vineyards, but also widely scattered. The Forest/Plantation class contains all mid-rise or high-rise trees, therefore besides the large forests also some orchards. The water class is dominated by the river.

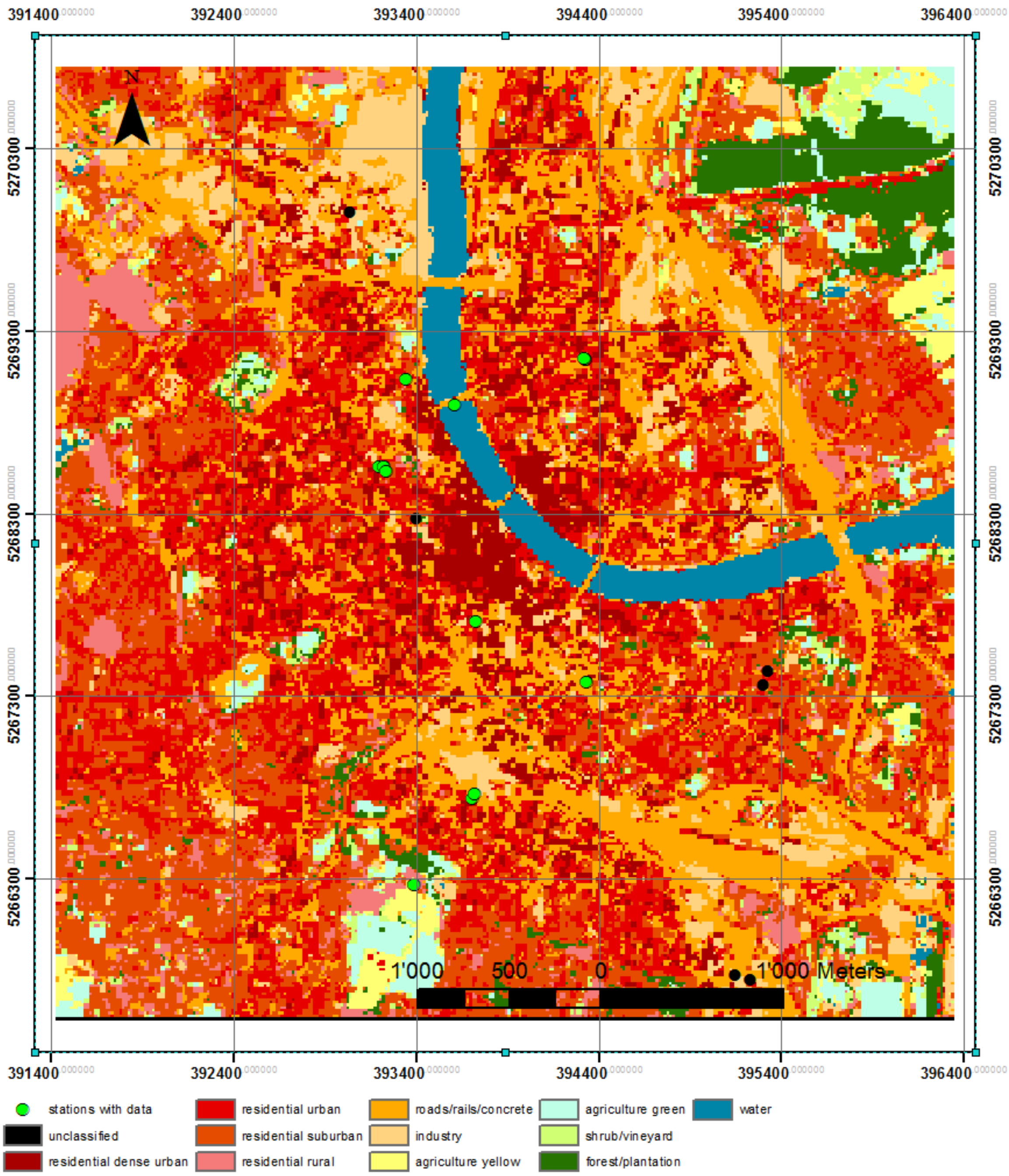

Figure 6. Land Use/ Land Cover (LULC) for 30 AUG 2015 (see text for methods and descriptions)

Table 4. Minimum stomatal resistance r_{sMIN} (adapted from Kato and Yamaguchi, 2007) and calculated stomatal resistance r_s for transpiring LULC classes from Equation (7)

LULC	r_{sMIN} (s m^{-1})	r_s (s m^{-1})
Agriculture yellow	500	551
Agriculture green	90	99
Shrubs/vineyard	100	110
Forest/Plantation	60	66
Water	0	0

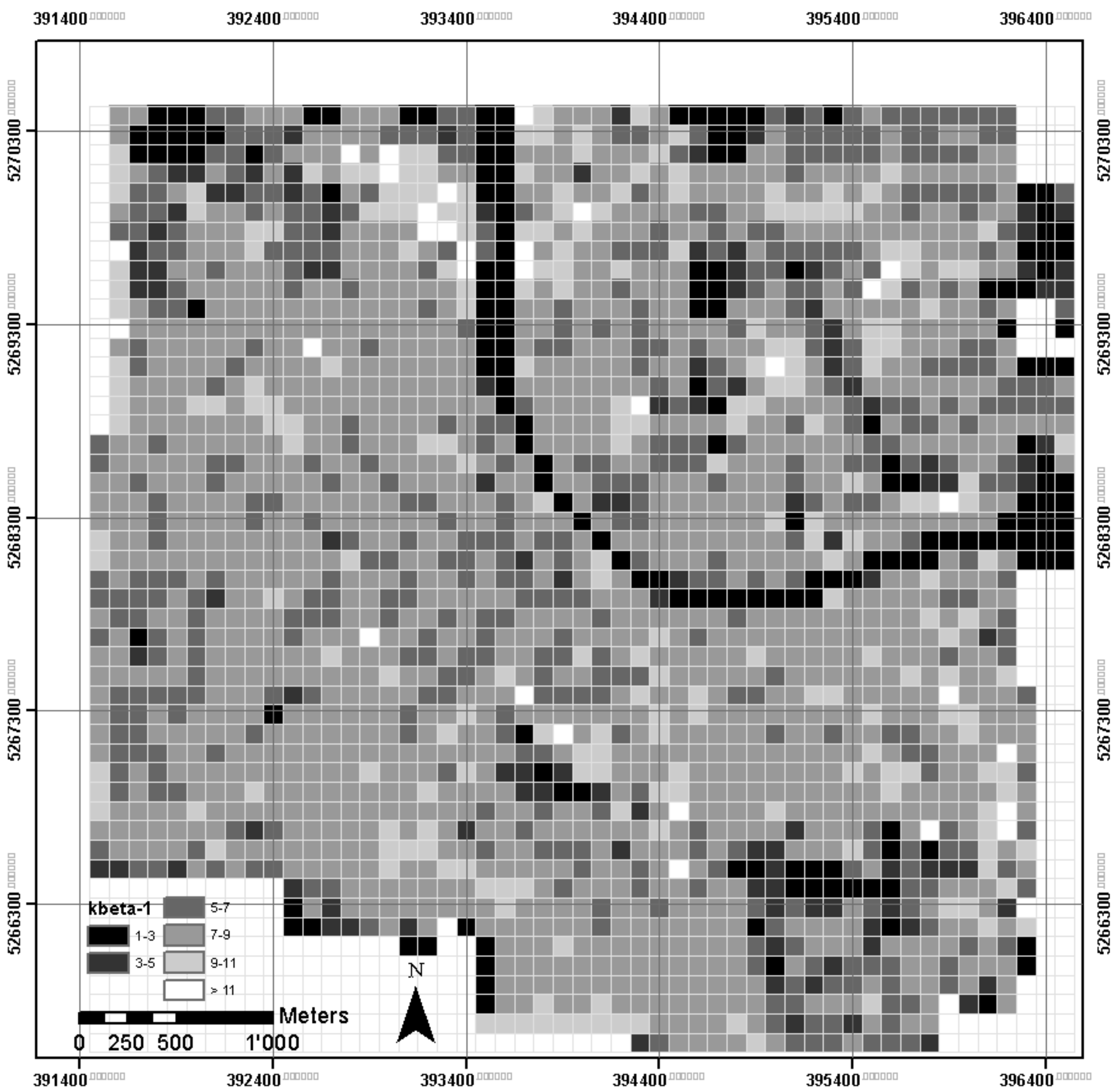

Figure 7. Dimensionless parameter kB^{-1} as calculated from Equation (7) for time of the overpass.

4.7 Sensible heat flux Q_H on a pixel base

Figure 9 shows the estimated sensible heat flux Q_H for the LANDSAT scene from 30 AUG 2015 1116 CET. The spatial pattern is dominated by the fractions of transpiring and impervious surfaces in a 100 m x 100 m pixel. The highest sensible heat fluxes are found in the most densely built-up regions with high surface temperatures and missing vegetation. Industrial areas particularly show high fluxes up to 300 W m^{-2} and more.

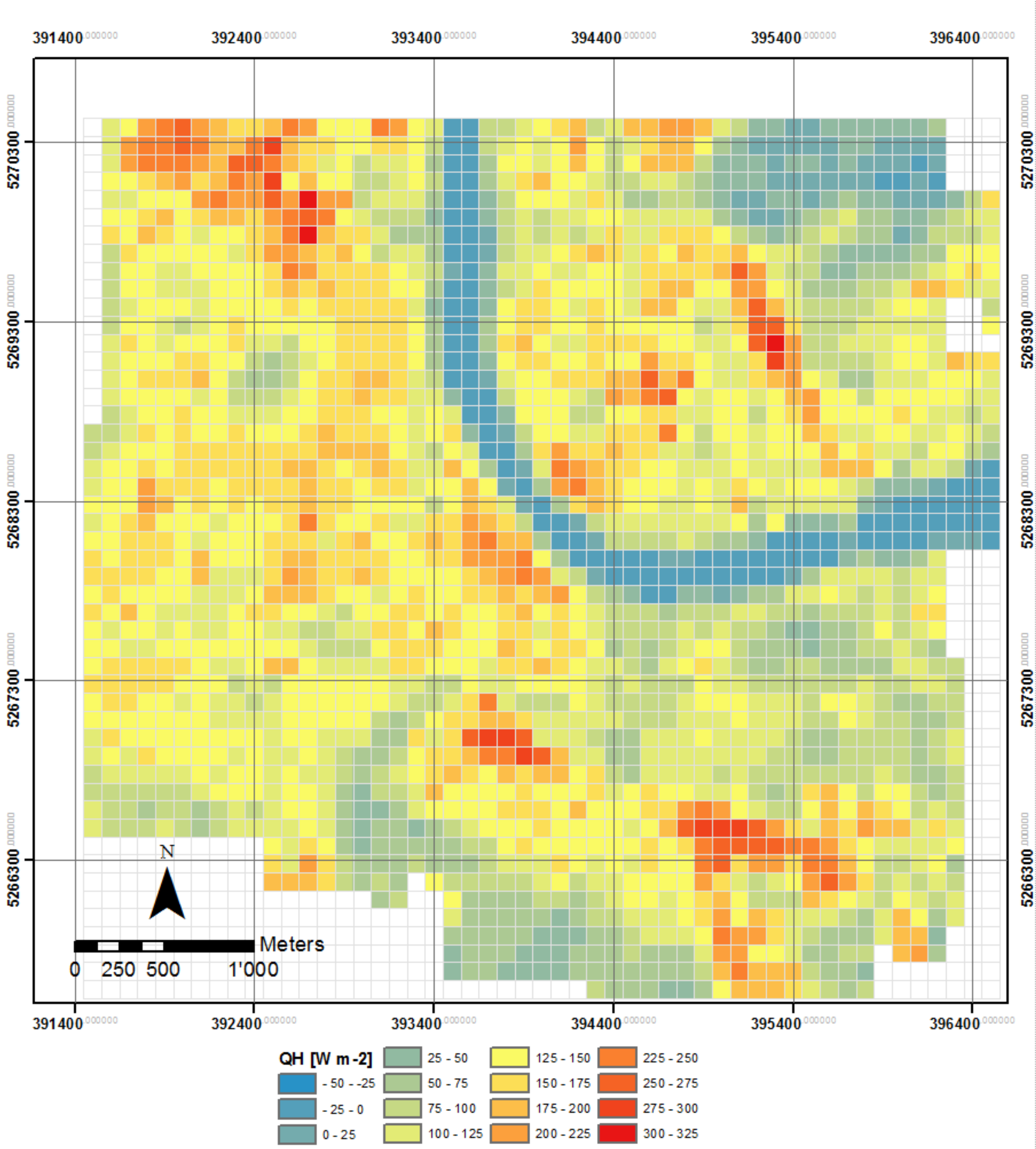

Figure 8. Sensible heat flux Q_H in W m^{-2} on 30 AUG 2015 at 1116 CET covering the central parts of Basel, Switzerland. White pixels have no roughness data available.

4.8 Latent heat flux Q_E on a pixel base

Figure 10 shows the estimated latent heat flux Q_E for the LANDSAT scene from 30 AUG 2015 1116 CET. The spatial pattern is dominated by the fractions of transpiring surfaces in a 100 m x 100 m pixel. Highest evapotranspiration rates are found over forests and parks with a considerable amount of trees. The Rhine River additionally shows increased evaporation compared to the densely built-up and impervious areas.

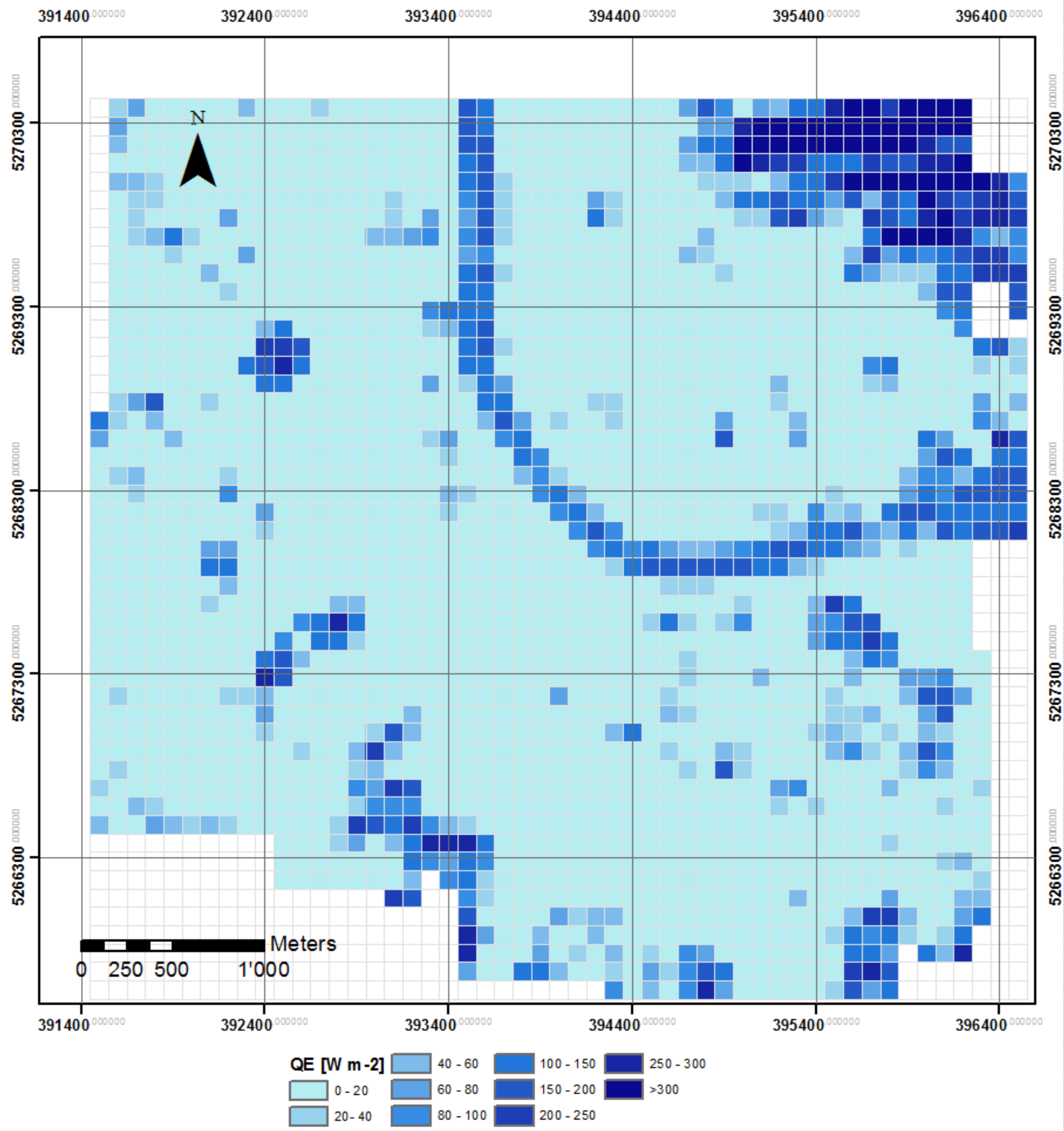

Figure 9. Latent heat flux Q_E in W m^{-2} on 30 AUG 2015 at 1116 CET covering the central parts of Basel, Switzerland. White pixels have no roughness data available.

5 CONCLUDING REMARKS AND FUTURE ACTIVITIES

The first estimates of spatially derived fluxes of sensible and latent heat show reasonable magnitudes and patterns. They compare well to eddy covariance (EC) measurements in the EC source area. A complete verification and uncertainty analysis is the subject of Deliverable D.6.2 and therefore out of the scope of this document. During the next months, data from the other case study cities (London and Heraklion) will be processed. The area in Basel will be extended as the needed base data (e.g. urban morphology) and measurements from the sensor networks become available. Future work includes a number of different activities related to the calculation of aerodynamic resistances including vegetation fractions from unmixing of Sentinel-2 data. Sensitivity studies of the applied algorithms will improve the accuracy of flux estimates. Additionally, the seasonal variation of stomatal resistances and the diurnal variation of kB^{-1} will be investigated.

The next milestone for WP6 is the main product of WP6 which will be delivered to WP7 for further processing: the Deliverable 6.2 “Report on cross-checking Q_H and Q_E fluxes with independent methods and measurements and the documentation of the database of the final Q_H and Q_E products” to be submitted on M18. Finally, by the end of the project (M36) the Deliverable D6.3 “Case studies measurements” will be submitted. It will be a database containing all in-situ measurements performed at all case study areas during the project’s lifecycle.

6 REFERENCES

Barsi, J.A., Barker, J.L., Schott, J.R., 2003. An Atmospheric Correction Parameter Calculator for a Single Thermal Band Earth-Sensing Instrument. IGARSS03, 21-25 July 2003, Centre de Congrés Pierre Baudis, Toulouse, France (http://atmcorr.gsfc.nasa.gov/)

Brutsaert, W., 1982. Evaporation into the Atmosphere. Springer Netherlands. ISBN: 978-90-481-8365-4

Dyer, A.J., 1974. A review of flux-profile relationships. Boundary- Layer Meteorol, 7, 363-372

González, A., Donnelly, A., Jones, M., Klostermann, J., Groot, A. and Breil, M., 2011. Community of Practice Approach to Developing Urban Sustainability Indicators. Journal of Environmental Assessment Policy and Management, 13, 1 - 27.

Grimmond, C. S. B., Oke, T. R. (1999). Aerodynamic properties of urban areas derived from analysis of surface form. Journal of Applied Meteorology, 38, 1262–1292

Högström, U., 1988. Non-dimensional wind and temperature profiles in the atmospheric surface layer: A re-evaluation. Boundary- Layer Meteorol, 42, 55-78

Kanda, M., Inagaki, A., Miyamoto, T., Gryschka, M., Raasch, S., 2013. A new aerodynamic parametrization for real urban surfaces. Boundary- Layer Meteorol, 148(2), 357-377

Kanda, M., Kanega, M., Kawai, T., Moriwaki, R., Sugawara, H., 2007. Roughness Lengths for Momentum and Heat Derived from Outdoor Urban Scale Models. J. Appl. Meteor. Climatol., 46, 1067 - 1079.

Kanda, M., Moriizumi, T., 2009. Momentum and heat transfer over urban-like surfaces. Boundary- Layer Meteorol, 131(3), 385-401

Kato, S., Yamaguchi, Y., Liu, C. C., Sun C. Y., 2008. Surface Heat Balance Analysis of Tainan City on March 6, 2001 Using ASTER and Formosat-2 Data. Sensors, 8, 6026 - 6044

Kohsiek W., De Bruin H.A.R., The H., van den Hurk B.J.J.M., 1993. Estimation of the sensible heat flux of a semi-arid area using surface radiative temperature measurements. Boundary-Layer Meteorol, 63, 213–230

Laben, C.A., Brower. B.V, 2000. US Patent 6,011,875, Google Patents, https://www.google.com/patents/US6011875

Lindberg, F., Grimmond, C.S.B., Onomura, S., Järvi, L., Ward, H., 2015. UMEP - An integrated tool for urban climatology and climate-sensitive planning applications. ICUC9 – 9 th International Conference on Urban. Toulouse, July 2015

Macdonald, R.W., Griffiths, R.F., Hall, D.J., 1998. An improved method for the estimation of surface roughness of obstacle arrays. Atmos Environ, 32, 1857–1864

Nadeau, D. F., Brutsaert, W., Parlange, M. B., Bou-Zeid, E., Barrenetxea, G., Couach. O., Boldi, M.-O., Selker, J. S., Vetterli, M., 2009. Estimation of urban sensible heat flux using a dense wireless network of observations. Environ. Fluid Mech., DOI 10.1007/s10652-009-9150-7.

Nishida, K. Nemani, R. R., Running, S. W., Glassy, J. M., 2003. An operational remote sensing algorithm of land surface evaporation. Journal of Geophysical Research, 108, doi: 10.1029/2002JD002062Noilhan, J., & Lacarrère, P. (1995). GCM grid-scale evaporation from mesoscale modeling. Journal of Climate, 8, 206−223

Offerle, B., Grimmond, C.S.B., Fortuniak, K., 2005. Heat Storage and Anthropogenic Heat Flux in Relation to the Energy Balance of a Central European City Centre. Int. J. Climatol., 25, 1405 - 1419.

Pigeon, G., Lemonsu, A., Masson, V., Durand, P., 2003: Sea–town interactions over Marseille—Part II: Consequences on atmospheric structure near the surface. Proc. of the 5th Int. Conf. on Urban Climate, O30.3, Łódz´, Poland, International Association for Urban Climate, 4 pp.

Pigeon, G., Legain, D., Durand, P., Masson, V., 2007. Anthropogenic heat release in an old European agglomeration (Toulouse, France). Int. J. of Climat., 27, 1969 - 1981.

Voogt, J.A., Grimmond, C.S.B., 2000. Modeling surface sensible heat flux using surface radiative temperatures in a simple urban area. Journal of Applied Meteorology, 39(19), 1679-1699

Xu, W., Wooster, M.J., Grimmond, C.S.B., 2008. Modelling of urban sensible heat flux at multiple spatial scales: A demonstration using airborne hyperspectral imagery of Shanghai and a temperature–emissivity separation approach. Remote Sensing of Environment, 112(9), 3493–3510

7 APPENDIX

7.1.1 Diurnal courses of meteorological variables on 30 AUG 2015

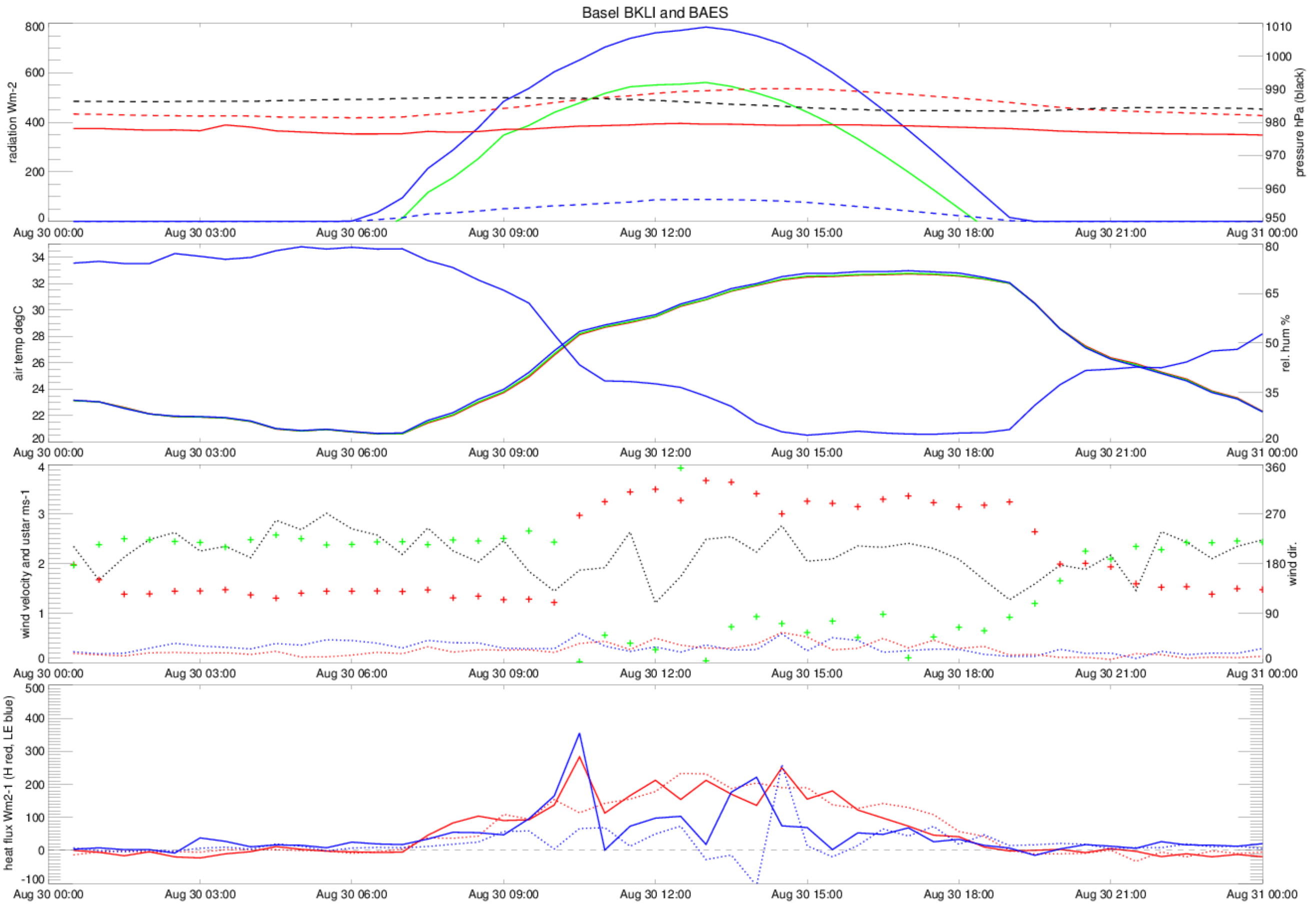

Figure A1: Flux towers BKLI (solid) and BAES (dotted)

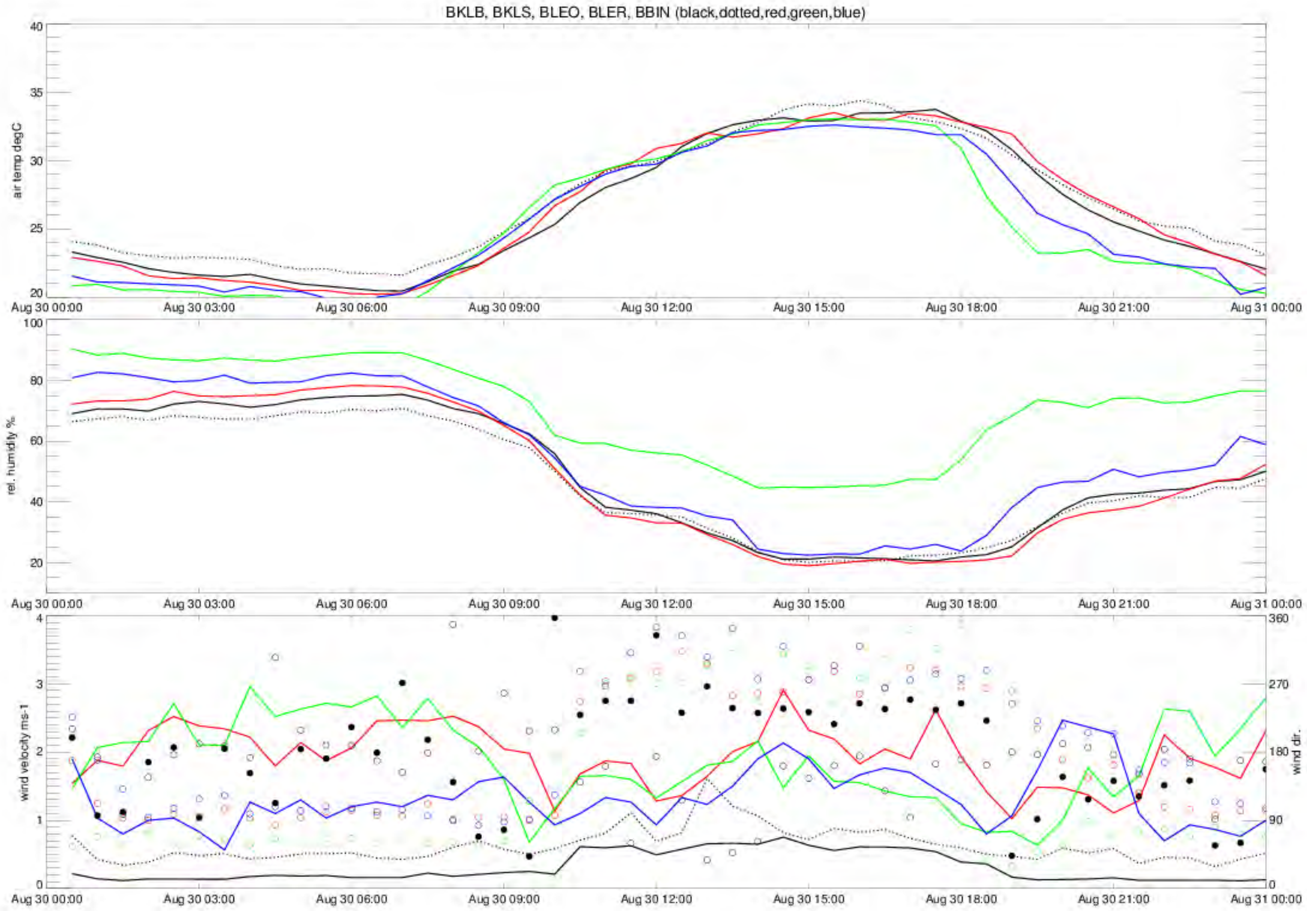

Figure A2: BKLB (black), BKLS (black dotted), BLEO (red), BLER (green), BBIN (blue)

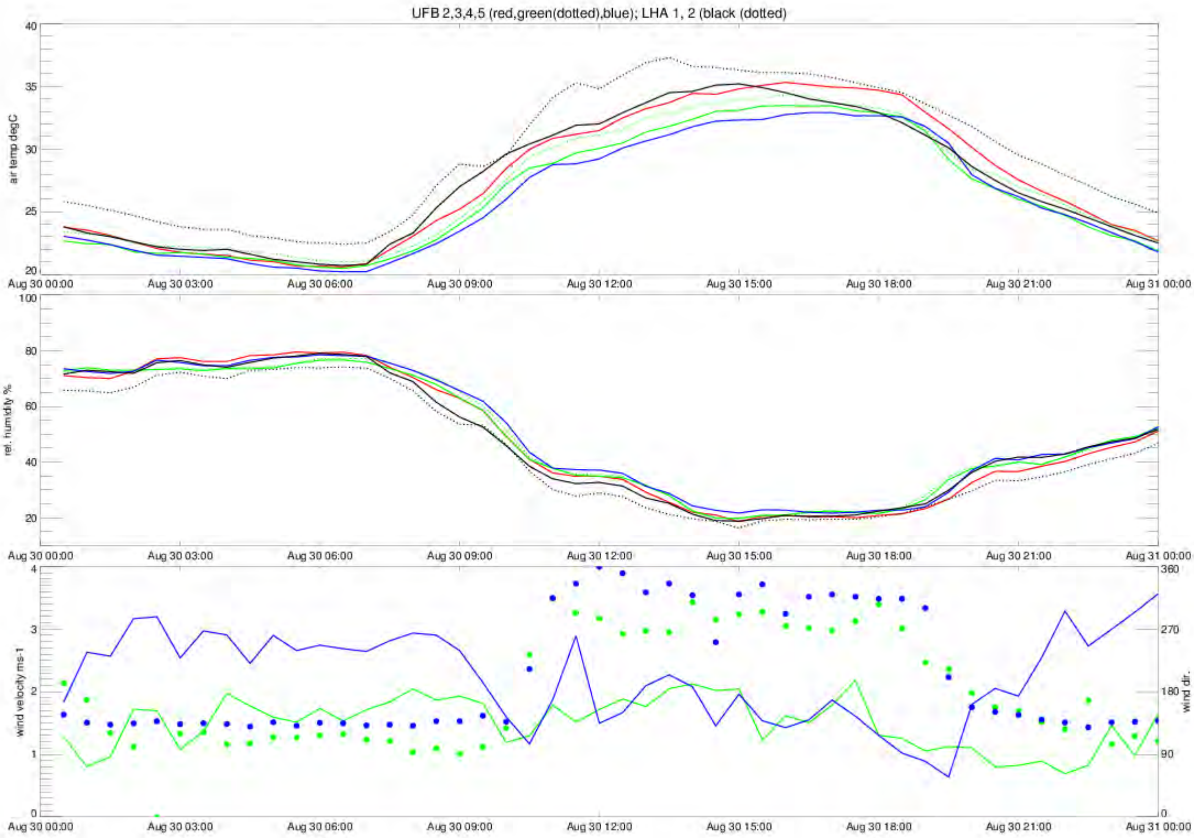

Figure A3: UFB2 (red), UFB3 (green), UFB4 (green dotted), UFB5 (blue), LHA1 (black), LHA2 (black dotted).